Shock Waves (2014) 24:501–513
DOI 10.1007/s00193-014-0511-x

ORIGINAL ARTICLE

Dynamic fragmentation of powders in spherical geometry

A. M. Milne · E. Floyd · A. W. Longbottom · P. Taylor

Received: 24 June 2013 / Revised: 16 May 2014 / Accepted: 27 May 2014 / Published online: 25 June 2014
© Springer-Verlag Berlin Heidelberg 2014

Abstract Experimental evidence from a wide range of sources shows that the expanding cloud of explosively disseminated material comprises of "particles" or fragments which have different dimensions from those associated with the original material. Photographic evidence shows jets or fingers behind these expanding fragments. Powders and liquids have often been used to surround explosives to act as blast mitigants; this is the main driver for our research. Other examples of areas where these features are observed include fuel air explosives and enhanced blast explosives as well as quasi-static pressure mitigation systems. In this paper, we consider the processes occurring when an explosive interacts with a surrounding layer of powder in spherical geometry. Results from explosive experiments designed to investigate the effects of powder grain size and powder fill-to-burster charge mass ratio (F/B) are presented and compared with results from numerical modelling to explore what determines the primary fragment size distribution resulting from explosive dissemination of a layer of material and when this process begins. The evidence clearly shows that the process starts during the first wave transit period of the powder material and, despite the surrounding material initially being a loose powder, shows the characteristics of a brittle fracture mechanism. Later time video evidence shows the same number of jets or fingers as are identified by X-rays of the early, primary fragmentation process. The number of fragments is only a very weak function of the initial grain size of the powder.

Communicated by C. Needham.

A. M. Milne (✉) · A. W. Longbottom
FGE Ltd., 83 Market St., St. Andrews, Fife KY16 8QL, UK
e-mail: alec.milne@fluidgravity.co.uk

E. Floyd · P. Taylor
AWE, Aldermaston, Reading RG74PR, UK

Keywords Modelling · Experiment · Blast · Fragmentation · Mitigation

1 Introduction

Blast effects from unconfined spherical charges have been studied for many years. The fireballs from unconfined spherical charges show characteristic Rayleigh–Taylor instability behaviour. The details of this spherical mixing layer have been discussed by Kuhl [1]. Milne et al. [2] noted that experimental evidence from a wide range of sources shows that the expanding cloud of explosively disseminated material comprises of "particles" or fragments which have significantly different dimensions from those associated with the original material. These authors considered both liquid and powder surrounds. Photographic evidence shows characteristic jets or fingers behind these expanding fragments. Frost and Zhang [3] have reviewed many of the processes occurring in heterogeneous blast including jet formation. Other examples are reported by Frost et al. [4] and in the book edited by Zhang [5]. There is broad interest in this phenomenon in a range of application areas such as enhanced blast explosives (EBX) and fuel air explosives (FAE). There are also other study areas where this topic is fundamental, such as mitigation of the blast pressure (both prompt and quasi-static) associated with detonation. In this paper, we consider generic results relevant to this wide range of applications but also consider some experiments initially driven by the prompt blast mitigation application, since a commonly used practical technique to reduce effects of blast from explosives is to surround the explosive with a layer of liquid, powder or a slurry mixture of the two. Drag is seen [6] as a potential mechanism to transfer energy from the blast wave to the disseminated particles or droplets so the size of particles, or

formation of jets is important in determining the efficiency of this mechanism.

This work is driven by observations that liquids, powders and slurries dispersed by explosives exhibit a late-time jetting phenomenon where the leading edge of the jet is an agglomerate of much smaller droplets or powder particulates acting as a larger particle which sheds debris as it propagates outwards. This paper concentrates solely on powder material surrounding the charge and investigates the effects of powder grain size as well as the effect of powder fill-to-burster charge mass ratio (F/B) on the formation of primary fragments. These experiments are diagnosed by X-radiography at early time and high-speed video for later times. If the grains of the powder acted as distinct elastic particles throughout the dissemination process one might expect individual grains to travel on distinct ballistic trajectories, but this is not what is observed. A mechanism for producing large-scale features, or primary fragments, which then travel ballistically needs to be defined. Milne et al. [2] showed that hydrodynamic instabilities (see for example Chandrasekhar [7]) could not explain the observed behaviour in both liquids and powders since the primary fragmentation process was observed by X-rays to occur well before the instability growth time. Frost et al. [8] have analysed experiments of different sizes and fill types in terms of a particle compaction Reynolds number ($Re = \rho U L/\mu_c$) where ρ, U, L are the density, velocity and length scales of the experiment and μ_c is an effective particle compaction viscosity. Dimensionally μ_c can be estimated as $\mu_c = \gamma_s c_s d_s$ where γ_s, c_s and d_s are particle density, sound speed and mean particle diameter, respectively. Their experiments showed correlations between the number of jets and the Reynolds number as defined above but they did not systematically change the particle size to influence Re in this work. This paper explicitly considers this aspect.

Xue et al. [9] have investigated the explosively driven dynamics of dry and wet sand using high-speed video. They find that the presence of even a small amount of liquid between the sand grains acts to increase the number of observed jets. They consider the jet formation as being determined by a balance of inertial and viscous forces and conclude that shear localization as opposed to interface instability is the dominant mechanism. They use essentially the same simple method as Milne et al. [2] to estimate break-up time. This paper augments high-speed video with X-ray data to improve upon this estimate and thus give extra evidence of the mode of break-up.

2 Previous work

Milne et al. [2] studied spherical systems both numerically and experimentally. Initial numerical modelling using simple equations of state found that, for all surrounds considered (liquid, powder and saturated powder), the detonation induces a spall layer followed by a release wave leading to an accretion layer which subsequently can break up and provides the initial conditions for subsequent jetting and finger formation.

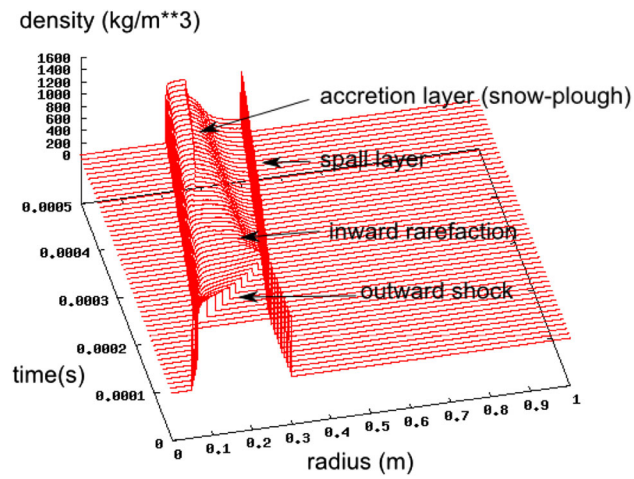

Fig. 1 Key early events in the water layer following central detonation with a water surround

We reproduce a calculation from this work in Fig. 1 which shows a wave plot through a water surround covering the first 0.5 ms of the event (in this case a 5-cm radius charge surrounded by a shell of water of outer radius 25 cm). As in [2], which describes these events in more detail, plotting of the waves in the explosive and the air is suppressed to allow one to clearly illustrate the behaviour in the water. Figure 2 shows line plots at key times from this calculation for clarity.

Numerical models for powders assumed that the grains acted as distinct elastic particles and that the release was elastic and thus had exactly the same features as seen in Fig. 1 for water. This paper addresses this assumption.

The key experimental conclusion was that primary fragmentation of the accretion layer occurs early in the process. The number of fragments observed in the radiographs was the same (within the observational error) as in the late-time videos. Once formed, these large fragments travel ballistically and shed debris along their trajectories. This paper investigates the early phase in more detail to try to determine more accurately when this primary fragmentation occurs.

From the earlier 1D studies in isolation one saw a deceleration of a two-fluid interface by a lighter fluid initially indicating that the Rayleigh–Taylor instability was a possible mechanism for formation of the initial fragments as clusters which subsequently erode aerodynamically. More detailed calculations (which allow for other interchange instabilities such as Rayleigh–Taylor, Richtmyer–Meshkov or Kelvin–Helmholz) taken in conjunction with the experimental data suggested [2] that one should eliminate Rayleigh–Taylor instability as a plausible cause since it occurs on too long

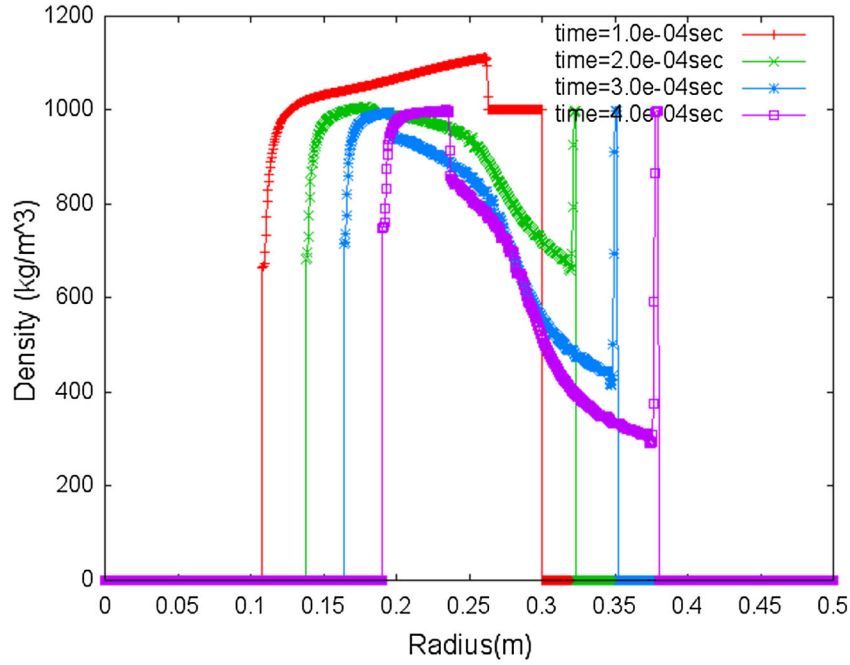

Fig. 2 Density profiles in the water from Fig. 1, at 0.1, 0.2, 0.3 and 0.4 ms

a timescale and does not lead to the primary fragmentation and jetting structure observed at early times. Similar calculations for these experiments confirm this conclusion.

Future work will concentrate on investigating a range of possible mechanisms which can lead to early fragmentation of liquid and powder shells surrounding a high explosive.

The limited database reported in Milne et al. [2] allowed one to hypothesise that the break-up mechanism for primary fragmentation occurs at a very early stage and that the primary fragment size is of the order of the width of the expanding shell at the time of break-up (i.e. not of the order of the original powder grain size which is much smaller). This paper addresses this hypothesis and also investigates the effect of grain size and powder fill-to-burster charge mass ratio on the primary fragmentation behaviour.

Table 1 Summary of experiment dimensions, fill-to-burster mass ratios, X-ray timings and video frame exposure times

Name	d_1 (m)	d_2 (m)	F/B	t_1 (μs)	t_2 (μs)	$t\exp_1$ (μs)	$t\exp_2$ (μs)
SPS2a	0.05	0.10	8	24	84	7	19
SPL2a	0.05	0.10	8	24	84	7	19
SPS4a	0.05	0.20	64	79	404	7	12
SPL4a	0.05	0.20	64	79	400	7	12
SPS2b	0.05	0.10	8	34	64	5	19
SPL2b	0.05	0.10	8	34	64	5	12
SPS4b	0.05	0.20	64	204	304	5	12
SPL4b	0.05	0.20	64	204	304	7	12

3 Experiments

Experiments where a sphere of explosive of diameter d_1 is surrounded by a spherical shell of glass beads of outer diameter d_2 are considered. Two diameter ratios (d_2/d_1) and two fill types are considered and diagnosed using a mix of X-radiography and high-speed video. We were practically limited to having only two distinct times for X-ray imaging in each shot so repeat shots were used to obtain different X-ray timings and to check for round-to-round repeatability using high-speed video.

Table 1 summarises the experiments reported in this paper using the naming convention that the first letter indicates the geometry used (in all cases in this paper spherical, so S). The second letter indicates the fill type (in all cases here powder, so P). The third letter indicates powder grain size (either small, S, or large, L). The number denotes the diameter ratio of the fill to the charge (2 or 4 in this series). The final letter indicates a repeat shot, a, b etc. and the two timings of the X-rays (in microseconds after detonation) for each experiment are denoted t_1 and t_2. The approximate fill-to-burster mass ratio for these dimensions is also given.

The experiments also have a case material of finite thickness (2 mm) but our definitions use d_1 as the outer diameter of the explosive (inner diameter of inner case) and d_2 as the outer diameter of the fill (inner diameter of the outer case).

One aim of the experiments is to use X-radiography to investigate the primary fragmentation process. The main error in the X-ray times is caused by the detonator cable getting shorter after each shot, resulting in a 20-ns increase

in the time between the detonator firing and the X-rays firing each time. Over the eight shots, this gives a maximum timing error of 0.14 μs. The exposure time for the radiographs is 30 ns and the error in the time difference between the two exposures is less than 2 ns.

Another part of the work is to use video recordings to follow the later stages and measure the form and number of the resulting jets or fingers. We used both a close-in view (with frame exposure times $t\exp_1$ in Table 1) and a wide view (with frame exposure times $t\exp_2$ in Table 1) to investigate the early and late stages of the expansion. Combining the X-ray and video results allows one to count the features and plot radius vs. time curves for their trajectories.

3.1 Experimental configurations

For simplicity of calculation and modelling, a spherical geometry was used; perturbations from spherical symmetry were kept to a minimum. Nylon 12 rapid prototype shells (density 0.9–0.95 g/cm^3) were designed using Unigraphics 3-D drafting software and then printed to support the explosive and the glass bead fill. The shell material was chosen to be light and thin so that shell interference with the fill expansion is minimised. Diagrams of these shells are shown in Figs. 3 and 4. The inner shell was designed to hold a 100 g sphere of PE4 and had an inner diameter of 5 cm. The rapid prototype Nylon 12 shell has a thickness of 2 mm. The two larger shells built to house the glass spheres have inner diameters of 10 and 20 cm meaning that the shell material has a mass of the order of 5 or 3 % of the fill masses, respectively. The dimensions of the shells (radii and thicknesses) are accurate to ±0.25 mm.

Glass beads were used as the powder fill material and two sizes were chosen from the range supplied by Potters Ballotini [10]. The larger spherical beads (manufacturers reference CP 3000) have a mean diameter between 30 and 50 μm, and the smaller spheres (CP 5000) have a mean diameter between 7 and 10 μm. These choices allow one to investigate the effect of a large variation in mean particle size.

As shown in Fig. 3, each hemisphere had a 2-cm flange containing male and female grooves to hold the two halves in place and 5.5-mm diameter holes so that M4 nylon nuts and bolts could be used to fix the hemispheres together. For the explosive part of the assembly all assembly components were weighed prior to filling. PE4 (a UK plastic explosive similar to C4) was moulded into the inner hemisphere of the male rapid prototype support, and into the corresponding spoon insert. An impression of an RP 83 detonator was then made into the PE4 in both sides. The shells were re-weighed to give the mass of PE4. We estimate that this procedure gives an accuracy of better than ±0.5 g for the explosive mass. The detonator lead was PVC taped to secure it firmly into the detonator channel, and the two halves of the inner

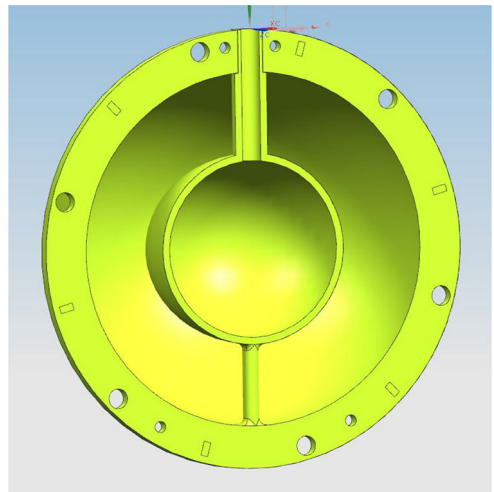

Fig. 3 Drawing of the (male) hemisphere of rapid prototype that supports the inner spoon

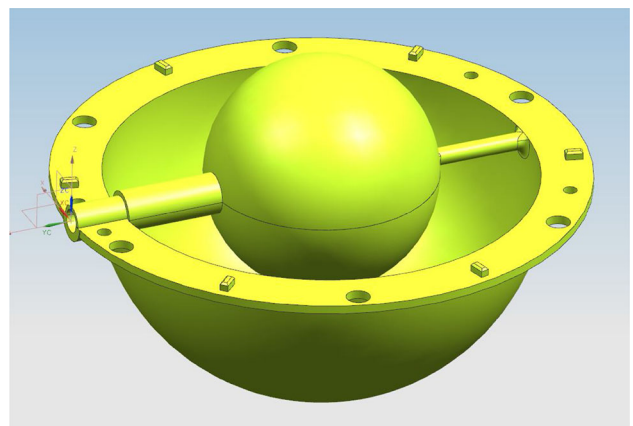

Fig. 4 Drawing of a hemisphere of rapid prototype with the spoon insert in place

shell were brought together and taped securely in place. The outer female hemisphere was then fixed into place with nylon bolts and the structure was placed in a supporting nest with its 1 cm filling hole and detonator cable port at the top. To fill the sphere uniformly with Ballotini spheres to the manufacturer's quoted densities the beads were poured in through a funnel while the whole experimental support was agitated. Each of the four experimental configurations was X-rayed to check for a homogeneous fill.

There are practical difficulties in filling and agitating a system containing explosives with fine powders. It is also more difficult to compact small spheres than large ones. A consequence of this is that there is a variability in the loading density of the powders from shot to shot.

Table 2 summarises the measured powder masses (accurate to ±1g) and densities (accurate to ±1.5 % as a result of the error bars for the shell dimensions) in each shot. One can see that the loading density can vary from as low as

Table 2 Powder masses and densities in each shot

Descriptor	Mass of PE4 (g)	Mass of mitigant (g)	Density of mitigant (g/cm^3)
SPS2a	93	597	1.35
SPS2b	94	727	1.65
SPS4a	94	5411	1.32
SPS4b	93	5511	1.34
SPL2a	93	692	1.57
SPL2b	94	613	1.39
SPL4a	93	6166	1.50
SPL4b	93	6586	1.60

1.32 g/cm^3 to 1.65 g/cm^3. The mean density for the small grain powder is 1.415 and 1.515 g/cm^3 for the larger grain powder. Future work will aim to address ways to reduce this variability.

The rapid prototype sphere was anchored through small holes in the rapid prototype flange by nylon cord into a wooden frame. The plane in which the two rapid prototype hemispheres are joined together was orientated along the line that separates the two pieces of film that are housed in each radiograph cassette. A laser level was used to align the shell with the X-ray sources and cassettes. The high-speed framing cameras were positioned at either side of the X-ray source stack.

4 Results and analysis

In this section, we summarise the data obtained and identify the analysis performed.

4.1 Radiograph results and analysis

Two 300kV X-ray sources with a Tungsten target and a Beryllium window were used to provide images of the expanding powder shells at two different times. The two X-ray sources were stacked vertically and the film cassettes were stacked securely opposite the X-ray source on a wooden stand. Two films were placed side by side in each cassette. The break between the films was located to coincide with the rapid prototype joint, capturing a hemispherical expansion on each film sheet. The distances measured between the X-ray sources, rapid prototype sphere and film plates result in a magnification of 1.36. One can also use this information to build up a radius vs. time ($r - t$) plot.

Figure 5 shows the time sequence of radiographs for the left-hand image of the 2:1 diameter ratio with the large glass beads (SPL2 in our notation).

The first and latest images were measured in one shot and the middle two were obtained in a subsequent shot. Some of the artefacts associated with the assembly system can be seen near the centre lines of the spheres.

In all of the results obtained in this series of experiments the left and right series show very similar behaviour. In all cases, no primary fragmentation structure is seen at the first time but a shell structure is clearly visible. Fine structure begins to be visible to the eye at the second time. Fine structure is seen at all subsequent times. One can observe that the number of fine structure features appears similar in all of the radiographs for each experimental configuration.

Figure 6 compares the last images in the time series for the 2:1 diameter ratio with the large and small glass beads. One finds that the number of features observed in both series is similar despite a fivefold variation in glass bead size.

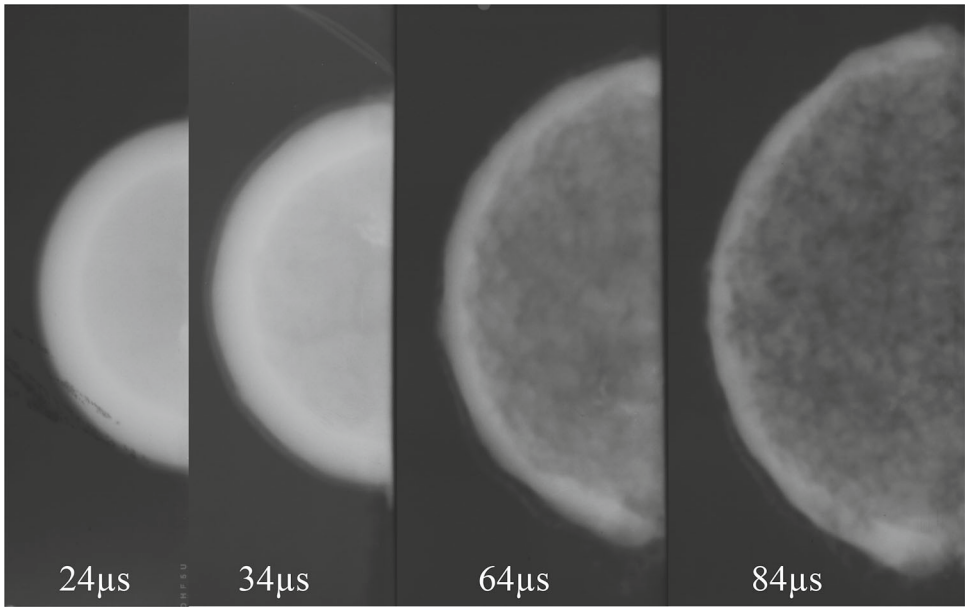

Fig. 5 Radiographs of SPL2 (*left image*) at various times

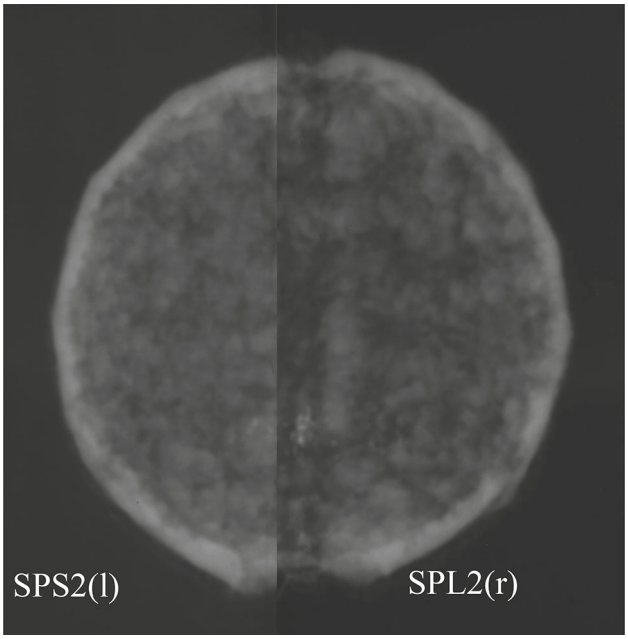

Fig. 6 Radiographs of SPS2 (*left image*) and SPL2 (*right image*) at 84 μs

Figure 7 illustrates the data from all four configurations using the left-hand images at the latest times.

The images show that the X-ray system used has difficulty in penetrating the larger and denser system. Comparing SPL4 and SPS4 again shows the number of features observed does not change significantly despite a large change in bead size.

4.2 Radius vs.time information

The outer surface of the shell is predominantly spherical with some perturbations for detonator cables. One can thus measure the outer radius of the sphere in each radiograph. The average of the values measured from the left and right images is plotted as green crosses on Fig. 8. One can also measure the inner radius of the fill material whose values are plotted as red plus signs in Fig. 9 which also shows the predictions from 1D spherical calculations (using the same numerical models described in [2]). The experimental results used only show the inner and outer edge of the shell of material, not any of the internal structure implied in the calculations. The error bars for the radii are smaller than the crosses in the figures.

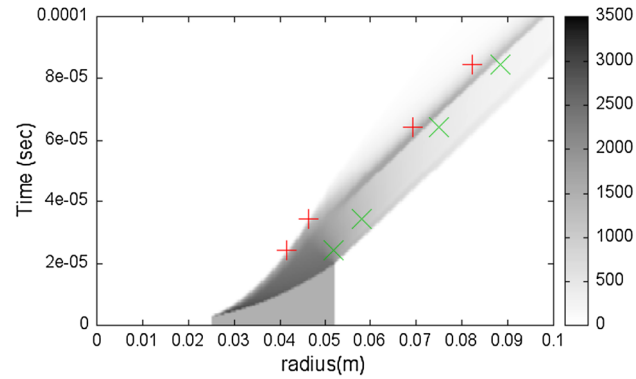

Fig. 8 Radius vs. time plot for SPL2 with recovery of compaction energy on expansion. *Red plus symbol* indicates the experimental location of inner surface and *green times symbol* the outer surface of the fill material. *Greyscale* shows density (kg/m^3) of powder

One can consider the hypothesis that the powder behaves as a mixture of distinct, elastic, incompressible particles effectively interacting as billiard balls. Such a powder does not support any tension and thus, after compression, is free to recover the energy associated with compaction by following the same path in expansion in P–V (pressure–volume) space as it did in compression.

In the absence of any evidence to the contrary our pre-shot calculations (and work in ref [2]) assumed all the compaction energy was recovered as the powder released back down the compaction curve as a result of the rarefaction wave from the outer surface. Figure 8 clearly shows that this model predicts a spall layer and an accretion layer as is seen with liquids but does not match the experimentally observed r–t plot. The work reported in [2] only had X-ray data at two times and these were consistent with an interpretation that the outer radius observed corresponded to the accretion layer introduced in Fig. 1. By doubling the number of observation times one can now see that this is no longer the correct conclusion.

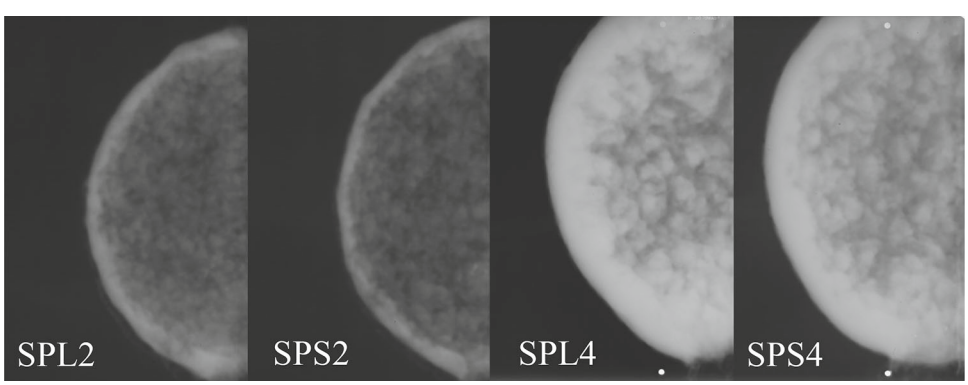

Fig. 7 Final radiographs in each series for each of the configurations studied

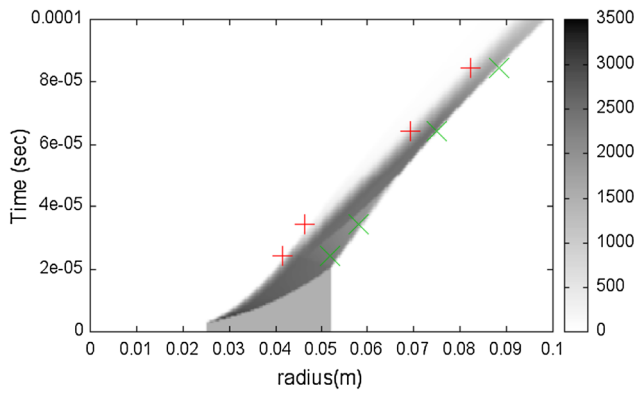

Fig. 9 Radius vs. time plot for SPL2 without recovery of compaction energy on expansion. *Red plus symbol* indicates the experimental location of inner surface and *green times symbol* the outer surface of the fill material. *Greyscale* shows density (kg/m^3) of powder

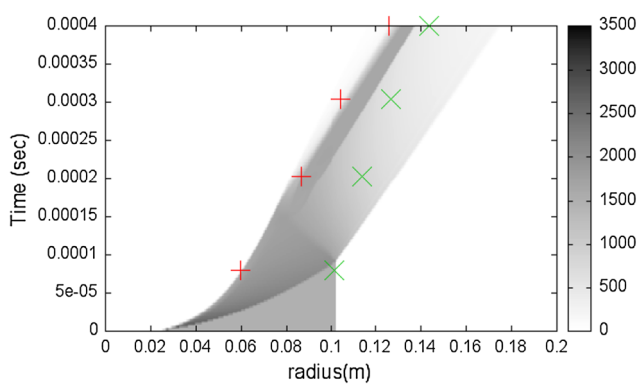

Fig. 10 Radius vs. time plot for SPL4 with recovery of compaction energy on expansion. *Red plus symbol* indicates the experimental location of inner surface and *green times symbol* the outer surface of the fill material. *Greyscale* shows density (kg/m^3) of powder

An alternative model for powders assumes that not all of the compaction energy is recoverable. This can happen for a variety of reasons. For example, the grains may fracture producing larger surface energy during the crushing process or some bonding force may be initiated. Here the loading and unloading curves are different with the final state on full unloading corresponding to a particle volume fraction greater than the value for the original unloaded bed. The slope of the unloading line may be determined by the bulk sound speed c_l of the material immediately prior to unloading (see for example Laine and Sandvik [11]).

Using this class of model one now sees in Fig. 9 that the calculation no longer predicts a spall layer and the inner and outer locations agree very well with the experiment.

The same behaviour is also seen for the larger particle size in Figs. 10 and 11.

This can guide developments of theories for the primary break-up process.

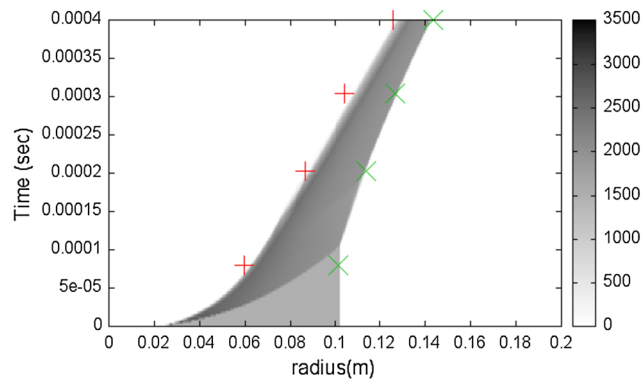

Fig. 11 Radius vs. time plot for SPL4 without recovery of compaction energy on expansion. *Red plus symbol* indicates the experimental location of inner surface and *green times symbol* the outer surface of the fill material. *Greyscale* shows density (kg/m^3) of powder

One can summarise these results by noting that in all cases (small and large beads at two different F/B ratios) some embryonic structure exists in the second radiograph of the series but none in the first. The calculations show that these timings bracket the time for the release wave to reach the inner surface. This provides clear experimental evidence that the onset of primary fragmentation occurs during the first wave transit times. Comparison of calculation with experiment gives clear evidence that not all of the compaction energy is recovered on this expansion. These conclusions are independent of the particle size used.

4.3 Analysis of scans

The X-ray photographic plates have been digitised to a bit depth of 32 and high resolution (so that the number of pixels over the individual features being observed is large). Public domain medical imaging software (ImageJ [12]) is used for further analysis to extract features from the X-ray images. The method used here analyses scans taken radially out from the centre of the images to pick out features. The X-ray image does not distinguish between front and back (it integrates the mass per unit area in any beam) and thus the number of peak features depends on the relative locations of the front and back fragments. One can minimise the effects of obscuration by varying the radial scan angle and choosing those scans which identify the largest number of clear features for counting (since overlapping fragments will only appear as a single feature). We have chosen to use this form of the data for quantitative analysis, being fully aware that there is a subjective element to this choice, since the number of features seen does vary as the radial scan angle is varied. We have found that this fact makes more sophisticated automated averaging procedures prone to significant error.

Figure 12 shows radial scans from the SPL2 series which are also typical of the scans from other the experimental con-

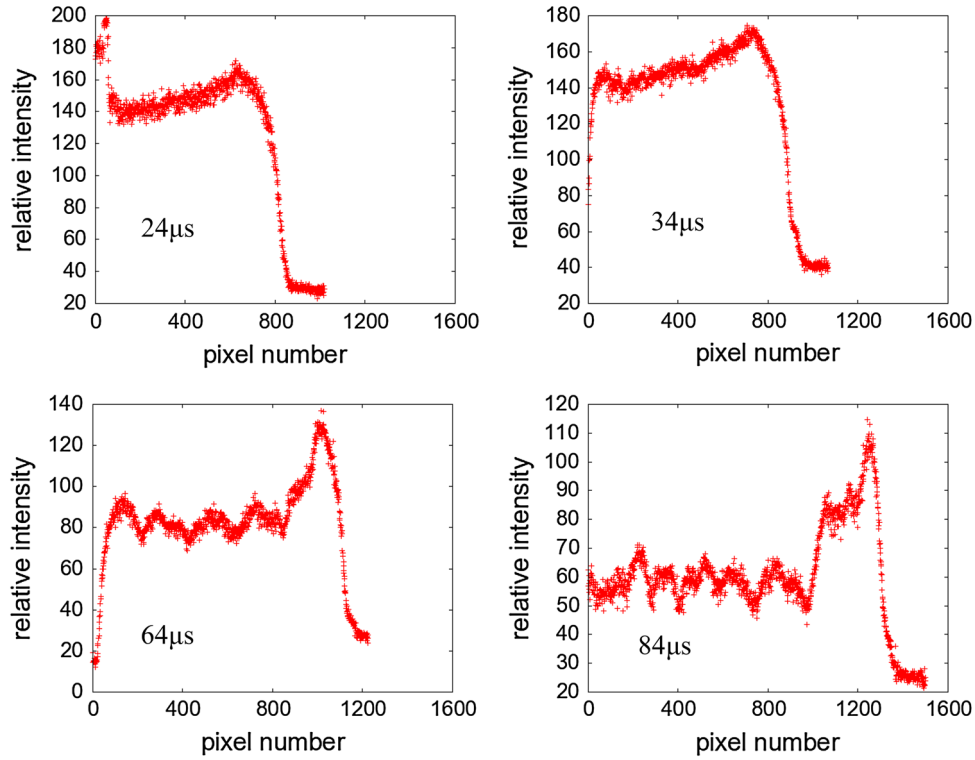

Fig. 12 Scans of radiographs (intensity v pixel number) of SPL2 (*left image*) at various times

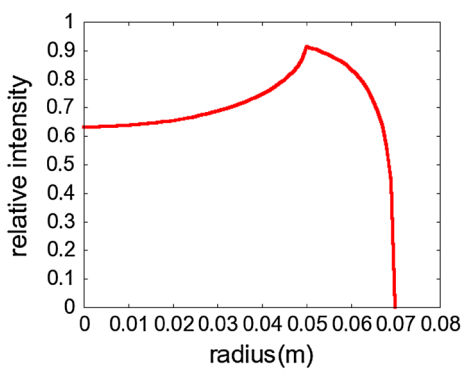

Fig. 13 Calculated relative attenuation as function of radius for a spherical shell of inner radius 0.05 m, outer radius 0.07 m and material with X-ray mean free path of 0.02 m

figurations being reported here. The earliest image shows an artefact at the centre but then exhibits the shape which is typical of a radiograph of a spherical shell. An X-ray image predominantly shows the areal mass (the integral of density along a ray path) and thus for a spherical shell the absorption is lowest at the centre (the lowest areal mass) and rises to a peak at the inside of the shell and then decreases to zero at the edge as shown in Fig. 13.

The early time scans thus allow a clear measurement of the inner and outer shell radii and show no evidence of any other structure. At the second time in the series one can still see the underlying shell structure but also (as in visual inspection of the radiograph) can begin to see some fine structure. At the third time one sees that the underlying shell structure has gone. The central portion is essentially a flat line with a distinct fine structure superimposed upon it. This is consistent with the spherical shell having broken up into distinct primary fragments. These overlap more near the edge of the view of the sphere so one observes higher absorption at the edge. The outer radius can easily be measured and the inner radius is taken to be defined by the thickness of the primary fragment at the edge. The same basic shape can be seen at the final time and in all cases where structure is seen one can count features and measure sizes.

Figure 14 compares the scans of the large and small glass beads for a 2:1 diameter ratio while Fig. 15 shows the same for a 4:1 diameter ratio.

In Fig. 15, we show representative scans from the SPL4 and SPS4 series.

4.4 Counting of features

Two methods have been used to count the number of features from the X-ray data and from the video data. The first uses the image directly. It is hard to identify distinct, non-overlapping features at the outer edge of the images. Instead, one can count the number of features from the image within a known solid angle and then, allowing for the fact that the X-ray sees both front and back, calculate number over whole sphere. In this paper, the number of features from the centre of the image out to half the outer radius is used. The second method

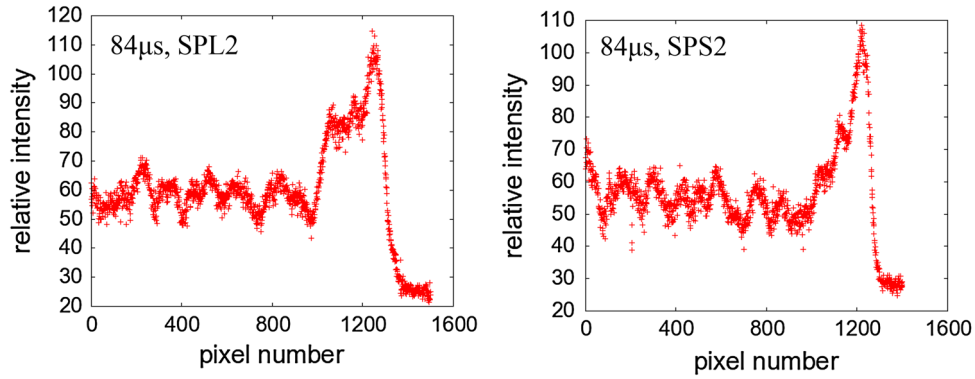

Fig. 14 Scans of radiographs (intensity v pixel number) of SPL2 and SPS2 at 84.3 μs

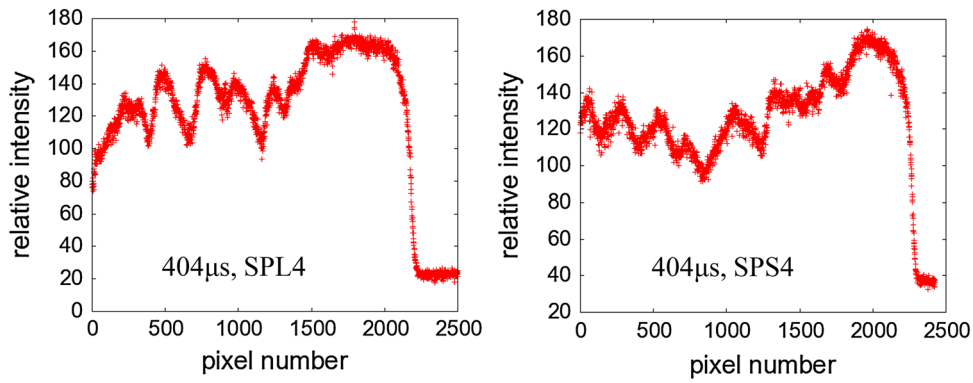

Fig. 15 Scans of radiographs (intensity v pixel number) of SPL4 and SPS4 at 404 μs

Table 3 Total number of primary fragments in the spherical shell counting from radiographs

	From image		From scan	
	l	*r*	*l*	*r*
SPL2	164	159	154	154
SPS2	261	250	215	250
SPL4	171	160	183	183
SPS4	253	230	215	215

counts the number of features along a radial scan and uses the observation that the features are of very similar size to estimate the solid angle associated with a single feature.

4.4.1 Counting from radiographs

It was noted above that the qualitative evidence from the radiographs was that the number of features was not changing significantly in time. Given that the overlapping of fragments in the front and back portions of the shell is more pronounced at early stages, it is more accurate to use the last images in each series as the basis for counting. Table 3 shows the number of features inferred using each of the methods introduced above.

One can see that the left and right images give broadly the same numbers. There is evidence from both methods that there are systematically slightly more features present in the experiments with the smaller grains (but not by a factor of five or more as would be expected if primary fragment size was proportional to grain size). For these shots, the diameter ratio for a given grain size does not seem to strongly influence the number of primary fragments.

4.4.2 Counting from video images

Two high-speed cameras were positioned either side of the X-ray source stack. A Phantom 16001 camera provided a close-up view for resolution of early time core break-up and jet formation, and a Phantom 122 camera provided a wider view that could track the jets to a later time. The camera views were the same for all the trials.

The cameras both have a resolution of 256 × 256 pixels, and for all images 12 bits were allocated to each pixel. The Phantom 16001 camera that provided the close-up view captured images at a rate of 133,333 frames per second (fps) and was used for all trials. The Phantom 122 camera that provided the wide view captured images at a rate of 50,000 fps for the first two trials, but the frame rate was increased to 80,000 fps for the remaining six trials. Table 1 records the frame exposure times for each shot.

The aim was to see the late-time jetting behaviour that is commonly observed in this class of experiment and to count the number of features observed in these images to compare

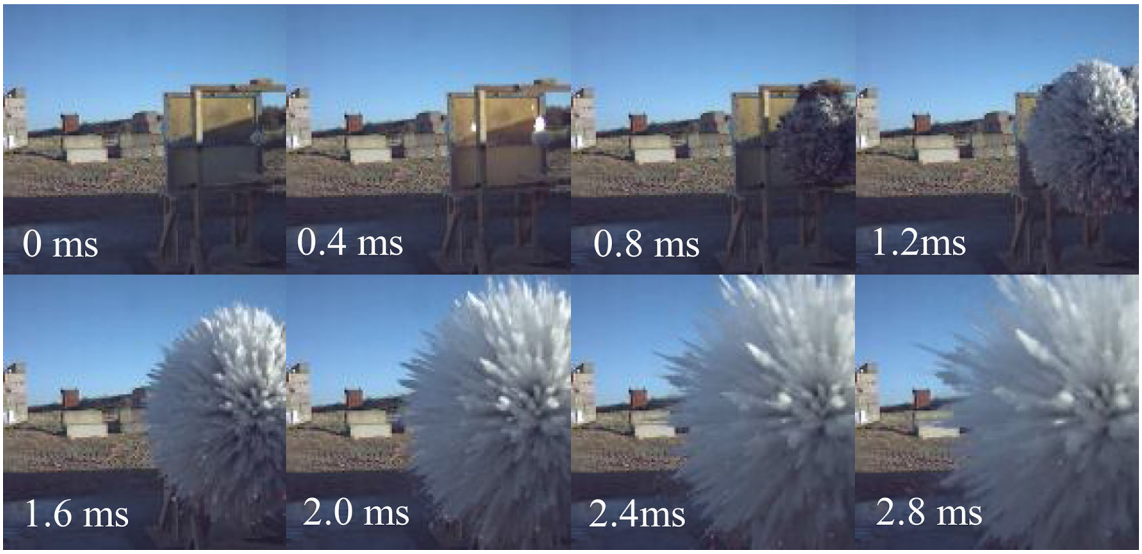

Fig. 16 Example of high-speed camera frames from a wide view of the SPS2a trial at various times

with the radiographic data. Figure 16 shows a sequence of frames from the wide view camera.

One can again use two counting methods which are broadly analogous to those used with the radiographic data.

Table 4 shows the number inferred from late times (2.8 and 5.2 ms for 2:1 and 4:1 diameter ratios, respectively) of each set of images from each of the cameras (1 and 2).

There is more variability between the two independent images than in the radiographic analysis. In the following section, we give an error analysis which will explain this.

An important general result that is consistent with [2] is that the number of jet features observed at late times in the video data is comparable with the number of primary fragments which are seen to form at very early times in the radiographic data.

Table 4 Number of primary fragments counting from video images from cameras 1 and 2

	From image		From scan	
	1	2	1	2
SPL2	249	183	244	180
SPS2	183	234	194	238
SPL4	234	234	240	194
SPS4	250	250	210	240

Table 5 Average number of primary fragments counted from image types

	Video average	Radiograph average
SPL2	214	157.75
SPS2	212.25	244
SPL4	225.5	174.25
SPS4	237.5	228.25

4.4.3 Error analysis

In both of the methods used for the radiographs (image and scan) one seeks distinct features in a subset of the data and uses the observed spherical symmetry to infer the number of features associated with the whole sphere. Typically the number of radial features counted in a scan is approximately 10 ± 1.

The total number over 4π varies as the square of the number of radial features so an error bar of the order of ± 20 % is an appropriate estimate.

The counting of features within a solid angle on a radiograph gives approximately 10–15 % error due to the size of features which overlap the boundary of the known solid angle.

The counting of features within a solid angle from a video image is less accurate than in the radiographs due to the higher complexity of the image. The error is 20 % due to the size of features compared with the bounding circle to count inside.

Counting the number of radial features is much less accurate for video images since one sees fingers or jet-like structures as opposed to large fragments; we estimate errors of the order of 25 %.

One can see that the error bars are large for all the counting methods. The numbers of features counted in radiographs are accurate to within ± 15 % while values ± 20–25 % are more appropriate for video data.

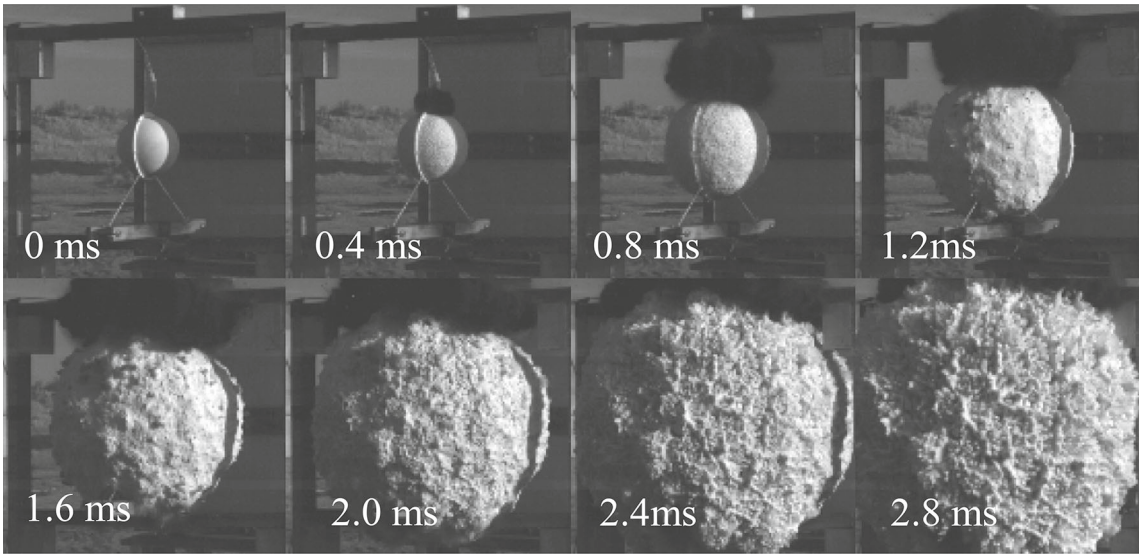

Fig. 17 Example of high-speed camera frames from a close view of the SPS4a trial at various times

4.4.4 Average results

The error estimates from counting preclude one from looking for too much fine detail in any interpretations. It is more appropriate to consider results averaged over the data for each experiment. Table 5 below gives the average number of primary fragments obtained from both methods for each series.

One can see that the video analysis has larger scatter and suggests that all experiments give the same number of fragments $\sim 220 \pm 50$

The average radiographic data suggests a mean of around 200 fragments. There is evidence that the larger grains give slightly fewer primary fragments than the smaller grains. Recall that the small grains were approximately 5 times smaller than the large grains so there were of the order of 125 times more small grains than large grains in each experiment. These large ratios put the small changes in observed numbers of primary fragments into clear context.

4.4.5 Close-in video analysis

The close view camera was fielded to give some extra optical information on the early stages of the expansion.

The early images of Fig. 17 show a lot of surface structure but none of this is of the same size as the features observed in the radiographs. The later images in the sequence show results representative of an early period, when a complex structure on the outer surface is apparent before a later phase (observed in the wider angle videos) takes over. In later phases (as observed in the wider angle videos) the same number of primary fragments as are apparent in the early radiographs can again be seen. One must thus be wary of inferring bulk behaviour from early time video evidence which can only see a surface layer.

4.5 Estimate of break-up time from number of fragments

Milne et al. [2] noted that there was good evidence that the primary fragmentation occurred at a very early stage associated with the time that the release wave from the outer surface reaches the inner surface of the fill. The current results support this. The earlier work also noted that by counting the number of fingers from a known mass of material one could infer a fragment size and we use the same method here. There is a degree of freedom here depending on assumed fragment shape but spheres and cubes can be considered as typical. The thickness of the expanding shell decreases with time and if one compares the predicted shell thickness with the inferred fragment size one can estimate break-up time as being the time when these two dimensions are equal.

Figure 18 plots the radius vs. time behaviour for SPL4 (both prediction and experiment). The simple method for estimating break-up time suggests it is 0.17 ms if one assumes cubic fragments or 0.14 ms if one assumes spheres. Both these estimates lie within the current limits which show that primary fragmentation has occurred between the first and second radiograph times.

Figure 19 shows the results of the same analysis for the smaller experiment (SPL2). The experimental results reported in this document show that the simple method to predict break-up time from a known number of late-time fingers appears to be accurate.

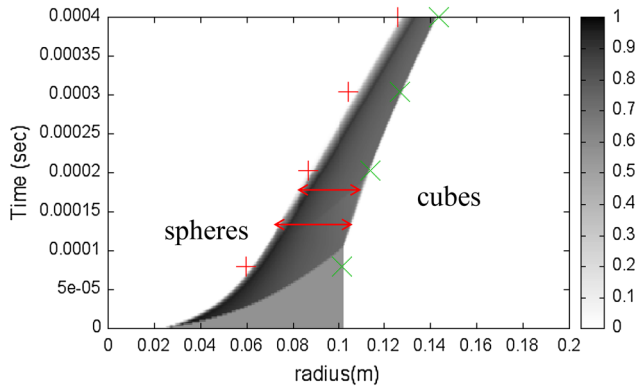

Fig. 18 Estimate of timing of primary fragmentation for SPL4. *Arrows* show dimensions of *cubes* or *spheres* required to match observed fragment numbers. *Red plus symbol* indicates the experimental location of the inner surface and *green times symbol* the outer surface of the fill material. *Greyscale* shows normalised density of powder

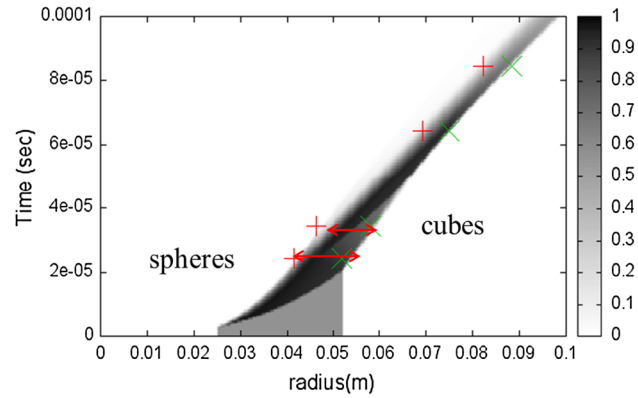

Fig. 19 Estimate of timing of primary fragmentation for SPL2. *Arrows* show dimensions of *cubes* or *spheres* required to match observed fragment numbers. *Red plus symbol* indicates the experimental location of the inner surface and *green times symbol* the outer surface of the fill material. *Greyscale* shows normalised density of powder

4.6 Density effects

Table 1 summarised the measured powder masses and densities in each shot. The variability in density influences the results of simple models for shell break-up time. If one decreases the loading density, the shell will be thinner at the time that the rarefaction wave reaches the inner surface. If this is indeed the time that determines primary fragment size one would expect smaller fragments (and thus more of them) for lower loading densities. The radiographic data suggested a small systematic increase in the number of primary fragments observed for small grain size particles. This variation was small compared with the variation in either grain size or number of grains. The data of Table 1 suggests that this observation may be a result of loading density effects.

At present there is insufficient evidence to prove or refute this conjecture but it emphasises the importance of trying to control initial loading density in future experiments.

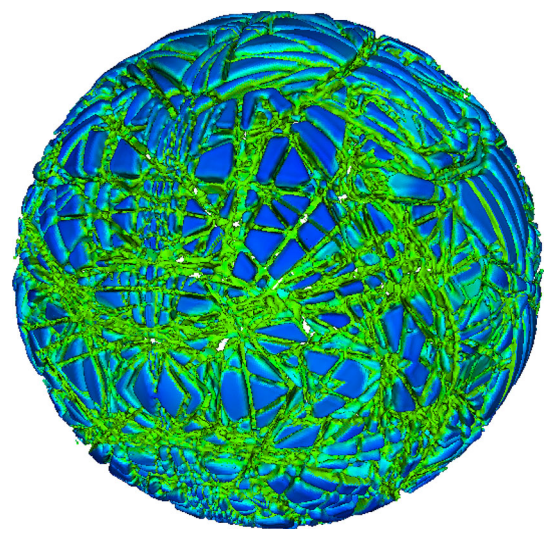

Fig. 20 Modelled crack distribution illustrated by a plot of surface density of the powder material at an instant corresponding to the time of the last radiograph for the 4:1 diameter ratio geometry

5 Modelling

Milne et al. [2] showed that the primary fragmentation process could not be explained by the growth of hydrodynamic instabilities such as Rayleigh–Taylor or Kelvin–Helmholtz since fragments were observed well before the growth time associated with these mechanisms.

The observed behaviour has features which are similar to brittle fracture due to crack formation, for example see Grady [13] for a detailed discussion of Mott fragmentation. The current dataset is not sufficient to identify a specific mechanism. Instead one can arbitrarily introduce a brittle fragmentation mechanism into numerical powder model by seeding a Mott distribution of flaws which can grow into cracks. Figure 20 shows the crack distribution implied by modelling at the time of the last radiograph for the 4:1 diameter ratio geometry.

One can process the above data to calculate the areal mass for rays through the shell and produce an approximation to a radiograph as shown in Fig. 21.

This analysis leads us to believe that some form of fracture mechanism is consistent with the observations presented here. We conjecture that the powder is explosively compacted into a brittle solid which then forms cracks as the shell expands. This conjecture is consistent with the observations that the primary fragmentation mechanism occurs during the first wave transit times. It is also consistent with the observation that the number and size of fragments are independent of the grain size (since compaction will fuse these materials into

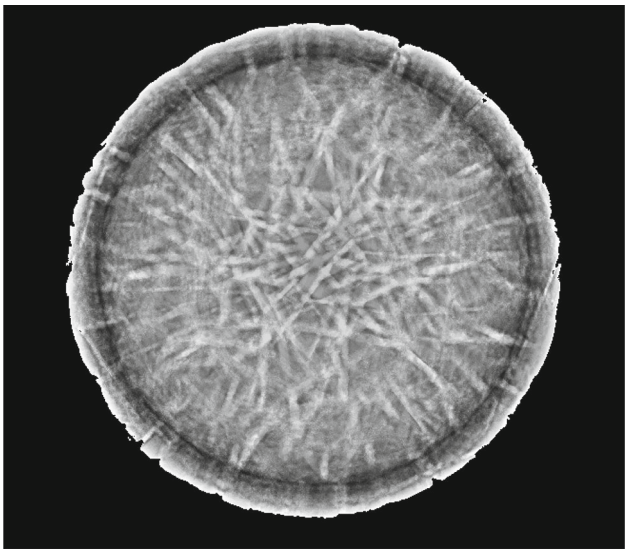

Fig. 21 Areal mass plot derived from Fig. 20 as an approximation to the last radiograph for the 4:1 diameter ratio geometry

a solid). This is also consistent with the observation that the radius time plot of the expansion of the shell is best modelled by assuming that the compaction energy is not recovered in the early stages of expansion. More work is needed to test this conjecture.

6 Conclusions

In this paper, the response of a spherical shell with a glass powder fill to the detonation of a central high-explosive sphere has been considered. The effects of powder grain size and the mass of powder compared with charge mass on the observed number of primary fragments and jets have been investigated.

This built on lessons learned from previous work in this area [2]. The main diagnostics were flash X-ray at four separate times in conjunction with high-speed video looking at wide angle expansion. One aim was to check if the number of features seen at early stages was the same as seen at late stages since the limited evidence to date suggested this was likely. Another aim was to identify when the primary break-up process started and to check the hypothesis that it occurred around the time that the release wave from the outer surface reached the inner surface of the fill.

The main conclusions from this work can be summarised as follows. The observed features are repeatable from shot to shot and primary fragments of uniform size are seen. The primary fragmentation process occurs very early in the shell expansion, around the time of the return of the release wave from the outer radius. The numbers of fragments are very similar at early time and late time. Qualitative evidence shows complex surface structures in intermediate time video data. The main drivers for the primary fragment size appear to be macroscopic flow and bulk material properties. The number of fragments has only a weak dependence on original grain size. There is evidence that this dependence may actually be a loading density effect.

Comparison of calculated and measured radius vs. time plots is consistent with incomplete recovery of compaction energy. Video data shows fragments shedding smaller particles in their wake at later times which suggests that any early time bonding is not permanent.

References

1. Kuhl, A.L.: Spherical mixing layers in explosions. In: Ray Bowen, L. (ed.) Dynamics of Exothermicity, pp. 291–320. Gordon and Breach (1996)
2. Milne, A.M., Parrish, C., Worland, I.: Dynamic fragmentation of blast mitigants. Shock Waves **20**, 41–51 (2010)
3. Frost, D.L., Zhang, F.: The Nature of Heterogeneous Blast Explosives. Julius Meszaros Memorial Lecture, Proceedings of the 19th International Symposium on Military Aspects of Blast and Shock, 1–6 Oct, Calgary, Canada (2006)
4. Frost, D.L., Ornthanalai, C., Zarei, Z., Tanguay, V., Zhang, F.: Particle momentum effects from the detonation of heterogeneous explosives. J. Appl. Phys. **101**(11), 113529 (2007)
5. Zhang, F.: Detonation of gas-particle flow. In: Zhang, F. (ed.) Heterogeneous Detonation, Shock Wave Science and Technology Reference Library, vol. 4, pp. 87–168. Springer, Berlin Heidelberg (2009)
6. Allen, R.M., Kirkpatrick, D.J., Longbottom, A.W., Milne, A.M., Bourne, N.K.: Experimental and numerical study of free-field blast mitigation. In: Furnish, M.D., Gupta, Y.M., Forbes, J.W. (eds.) Shock Compression of Condensed Matter-2003, pp. 823–826. American Institute of Physics, Melville (2004)
7. Chandrasekhar, S.: Hydrodynamic and Hydromagnetic Instability. Clarendon Press, Oxford (1961)
8. Frost, D.L., Gregoire, Y., Goroshin, S., Zhang, F.: Interfacial Instabilities in Explosive Gas-Particle Flows, Proceedings of the 23rd International Colloquium on the Dynamics of Explosions and Reactive Systems, Univ. of California, Irvine, USA (2011)
9. Xue, K., Li, F., Bai, C.: Explosively driven fragmentation of granular materials. Eur. Phys. J. E. **36**, 95 (2013)
10. www.pottersbeads.com
11. Laine, L., Sandvik, A.: Derivation of mechanical properties for sand. In: Proceedings of 4th Asia Pacific conference on Shock and Impact loads on structures, pp. 361–368. C.I. Premier PTE Ltd, Singapore (2001)
12. http://rsb.info.nih.gov/ij/
13. Grady, D.E.: Fragmentation of Rings and Shells: The Legacy of N. F. Mott. Springer, Berlin (2006)